

Electrochemical Stability of Metastable Materials

Arunima K. Singh, Lan Zhou, Aniketa Shinde, Santosh K Suram, Joseph H. Montoya, Donald Winston, John M. Gregoire, and Kristin A. Persson

Chem. Mater., **Just Accepted Manuscript** • DOI: 10.1021/acs.chemmater.7b03980 • Publication Date (Web): 24 Oct 2017

Downloaded from <http://pubs.acs.org> on October 24, 2017

Just Accepted

“Just Accepted” manuscripts have been peer-reviewed and accepted for publication. They are posted online prior to technical editing, formatting for publication and author proofing. The American Chemical Society provides “Just Accepted” as a free service to the research community to expedite the dissemination of scientific material as soon as possible after acceptance. “Just Accepted” manuscripts appear in full in PDF format accompanied by an HTML abstract. “Just Accepted” manuscripts have been fully peer reviewed, but should not be considered the official version of record. They are accessible to all readers and citable by the Digital Object Identifier (DOI®). “Just Accepted” is an optional service offered to authors. Therefore, the “Just Accepted” Web site may not include all articles that will be published in the journal. After a manuscript is technically edited and formatted, it will be removed from the “Just Accepted” Web site and published as an ASAP article. Note that technical editing may introduce minor changes to the manuscript text and/or graphics which could affect content, and all legal disclaimers and ethical guidelines that apply to the journal pertain. ACS cannot be held responsible for errors or consequences arising from the use of information contained in these “Just Accepted” manuscripts.

Electrochemical Stability of Metastable Materials

Arunima K. Singh,^{*,†} Lan Zhou, Aniketa Shinde, Santosh K. Suram,[‡] Joseph H. Montoya,[¶] Donald Winston,[¶] John M. Gregoire,[‡] and Kristin A. Persson^{*,§,||}

Joint Center for Artificial Photosynthesis, Lawrence Berkeley National Laboratory, Berkeley, California 94720, U.S.A. , Joint Center for Artificial Photosynthesis, California Institute of Technology, Pasadena, CA 91125, USA, Lawrence Berkeley National Laboratory, Berkeley, CA 94720, USA, Environmental Energy Technologies Division, Lawrence Berkeley National Laboratory, Berkeley, CA 94720, USA, and Department of Materials Science and Engineering, University of California, Berkeley, CA 94720, USA

E-mail: arunimasingh@lbl.gov; kapersson@lbl.gov

Abstract

We present a first-principles based formalism to provide a quantitative measure of the thermodynamic instability and propensity for electrochemical stabilization, passivation or corrosion of metastable materials in aqueous media. We demonstrate that this

^{*}To whom correspondence should be addressed

[†]Joint Center for Artificial Photosynthesis, Lawrence Berkeley National Laboratory, Berkeley, California 94720, U.S.A.

[‡]Joint Center for Artificial Photosynthesis, California Institute of Technology, Pasadena, CA 91125, USA

[¶]Lawrence Berkeley National Laboratory, Berkeley, CA 94720, USA

[§]Environmental Energy Technologies Division, Lawrence Berkeley National Laboratory, Berkeley, CA 94720, USA

^{||}Department of Materials Science and Engineering, University of California, Berkeley, CA 94720, USA

1
2
3
4 formalism can assess the relative Gibbs free energy of candidate materials in aqueous
5 media as well as their decomposition products, combining solid and aqueous phases,
6 as a function of pH and potential. Based on benchmarking against 20 stable as well
7 as metastable materials reported in the literature and also our experimental charac-
8 terization of metastable triclinic-FeVO₄ we present quantitative estimates for the rel-
9 ative Gibbs free energy and corresponding aqueous regimes where these materials are
10 most likely to be stable, form inert passivating films or steadily corrode to aqueous
11 species. Furthermore, we show that the structure and composition of the passivating
12 films formed on triclinic-FeVO₄ are also in excellent agreement with the Point Defect
13 Model, as proposed by the corrosion community. An open-source web-app based on the
14 formalism is made available at <https://materialsproject.org>.
15
16
17
18
19
20
21
22
23
24
25
26

27 Introduction

28
29
30 The economic cost of environmental degradation of materials has been estimated to be over
31 200 billion dollars in the US economy alone.¹ Corrosion management, improvement in perfor-
32 mance and an increased operational life of materials for household appliances, infrastructure,
33 vehicles and manufacturing calls for an improved understanding of materials stability un-
34 der varying alkalinity, humidity, temperature and pollutant conditions. Further, aqueous
35 media-based electrochemical processes such as water purification and catalysis routinely op-
36 erate devices at finite potentials and pH where materials stability is strikingly different from
37 ambient conditions.
38
39
40
41
42
43
44
45

46
47 A concise equilibrium thermodynamics-based understanding of elemental corrosion in
48 aqueous media can be accurately obtained from the so-called Pourbaix diagrams which in-
49 dicate the potential and pH ranges where the different multicomponent oxidation states of
50 materials exist. Marcel Pourbaix and others have collected thermodynamic data for re-
51 actions involving metals, their ions, their oxides and occasionally sulphides, providing the
52 electrochemical phase diagrams for ca. 85 elements in the periodic table.²⁻⁴ While the elec-
53
54
55
56
57
58
59
60

1
2
3 trochemical stability of elements has been studied extensively, only a small fraction of binary
4 materials and seldom ternary and higher-component materials have been investigated exper-
5 imentally.
6
7

8
9 Recently, Persson *et al.*, used first-principles density-functional theory (DFT)-based ther-
10 modynamic energies of solids in conjunction with experimentally available ion and aqueous
11 specie energies to predict Pourbaix diagrams of n -component materials ($n = 1$ to ∞).⁵ This
12 formalism has reproduced the thermodynamic electrochemical stability of all experimentally
13 investigated $n = 1$ systems, and to date, successfully predicted the electrochemical stabil-
14 ity of several complex materials such as: $\text{Mn}_2\text{V}_2\text{O}_7$,⁶ MnNiO_3 , Cu–V–oxides,⁷ and nano-
15 clusters.⁸ In principle, Pourbaix diagrams account for materials only at thermodynamic
16 equilibrium, providing no insight into the electrochemical stability of metastable materials
17 which find practical applications in many commercial applications and research such a steels,⁹
18 ceramics,¹⁰ photocatalysis¹¹ and optoelectronics.¹² Further, among the 29,902 unique bulk
19 crystalline phases reported in the Inorganic Crystal Structure Database (ICSD),¹³ the first-
20 principles-based, zero-temperature Materials Project database computations predict that
21 $50.5 \pm 4\%$ (15,097) of the experimentally synthesized structures are metastable solid state
22 phases.¹⁴
23
24
25
26
27
28
29
30
31
32
33
34
35
36
37

38 We expand the formalism of Persson *et al.* to enable the evaluation of the relative Gibbs
39 free energy of metastable materials as a function of pH, potential, temperature and concen-
40 tration of aqueous species. Note that while this formalism accounts for the experimentally
41 measured entropy of several gases, water and all aqueous species, we neglect the entropic
42 contributions for the solids towards Gibbs free energies since the solid-solid entropy differ-
43 ences are likely to be orders of magnitude smaller than the enthalpic contributions at room
44 temperature.¹⁵ We demonstrate that materials with decomposition Gibbs free energies as
45 high as 0.5 eV/atom have been reported as stable against corrosion due to self-passivation
46 and formation of more stable solid state surface phases. An excellent correlation is found
47 between the Gibbs free energy and propensity of 20 materials (including GaP, $\text{Zn}(\text{FeO}_2)_2$, Si,
48
49
50
51
52
53
54
55
56
57
58
59
60

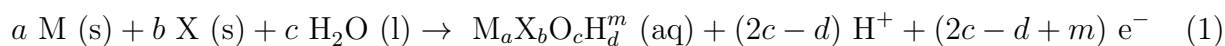
1
2
3
4
5
6
7
8
9
10
11
12
13
14
15
16
17
18
19
20
21
22
23
24
25
26
27
28
29
30
31
32
33
34
35
36
37
38
39
40
41
42
43
44
45
46
47
48
49
50
51
52
53
54
55
56
57
58
59
60

WSe₂, GaAs, Fe₂O₃, WO₃ and TiO₂) reported in the experimental literature, to be stable, passivate or corrode. In addition, we grow the metastable triclinic-FeVO₄ phase and show that the electrochemical response of FeVO₄ is in excellent agreement with the computational predictions with respect to both the stability and composition of the self-passivated layers, as applicable. The instability landscape reported in this article provides a critical guide towards environmental degradation management as well as design of metastable materials or protective films in materials of all classes for aqueous media-based applications. Further, we suggest that an *a priori* knowledge of the passivation layer composition can aid the kinetic and phenomenological Point Defect Model¹⁶ to predict the microstructure, passivation layer thickness and the kinetic stability of self-passivating films.

The formalism is made available through a user-friendly web-based app which allows for the generation and assessment of the metastability of over 69,000 materials; including estimation of pH, concentration and potential dependent composition of possible passivation layers, available at <https://materialsproject.org>.

Methods

Mapping Pourbaix diagrams for multi-component systems requires the knowledge of equilibrium redox reactions as well as the standard state reaction Gibbs free energy of each redox reaction, $\Delta_r G^\circ$. For example, a binary M-X system in aqueous media can result in a redox reaction such as,



where a, b, c, d are the stoichiometric coefficients of M, X, O and H, respectively, and m is the charge on the aqueous species $\text{M}_a\text{X}_b\text{O}_c\text{H}_d^m$ which could be positive, negative or zero. The number of competing redox reactions scales rapidly with the number of elements considered to compute the Pourbaix diagram. For instance, for a Fe-V system, there are 11 experimen-

tally reported Fe-containing and 14 V-containing (positively charged, negatively charged or neutral) aqueous species, along with 14 ground state solids containing one or more of Fe, V or O elements. At equilibrium, the Nernst equation can be used to relate the cell potential, E^o , to the reaction Gibbs free energy, $\Delta_r G$, for each possible redox reaction. For instance,

$$-\nu F E^o = \Delta_r G = \Delta_r G^o + R T \ln Q \quad (2)$$

$$= \Delta_r G^o + R T \ln \left[\frac{(a_P)^p \cdot (a_{H^+})^h}{(a_R)^r \cdot (a_{H_2O})^w} \right] \quad (3)$$

$$= \Delta_r G^o + 2.303 R T \log \left[\frac{(a_P)^p}{(a_R)^r \cdot (a_{H_2O})^w} \right] - 2.303 h R T \text{ pH} \quad (4)$$

Where T is the temperature, F is the Faraday constant, R is the ideal gas constant, $\text{pH} = -\log(H^+)$, $\nu = (2c - d + m)$ is the number of electrons, $a_R^r = a_{M(s)}^a \cdot a_{X(s)}^b$ is the activity of the reactants, $a_P^p = a_{M_a X_b O_c H_d^m}$ is the activity of the products, $a_{H_2O}^w = a_{H_2O}^c$ is the activity of water, and $a_{H^+}^h = a_{H^+}^{(2c-d)}$ is the activity of hydrogen ions for the reaction in Eq. 1. In principle, identifying the redox reaction that minimizes the difference between the contribution from the cell potential and the reaction Gibbs free energy, $\min(\Delta_r G + \nu F E^o)$, is sufficient to identify the range of pH and E where a particular solid or ionic species is stabilized over others for a given temperature, concentration of ions and stoichiometry of elements under consideration.

However, the lack of complete knowledge of possible redox reactions is the limiting factor in this analysis. In previous efforts, computed crystalline solid energies have been combined with experimentally measured free energies of aqueous species, which are readily available in thermodynamic databases.⁵ A thorough description of the scheme of reference energies which allows for the combination of experimental and computational thermodynamic data can be found in Ref. 5. Further, computational materials data is available in larger and more comprehensive quantities than ever before through efforts like The Materials Project,¹⁷ OQMD,¹⁸ and aflowlib.¹⁹ The experimentally measured energies of aqueous species,^{2,3,15,20,21} total 362, corresponding to 80 elements in the periodic table, are also available through the

1
2
3
4 Materials Project (MP) API.²² Among the 69,640 currently available materials in the MP
5
6 database, 34,913 materials correspond to compounds in the ICSD, 23,776 are ground states,
7
8 and the intersection of these sets contains 18,993 compounds. In conjunction with 362 ionic
9
10 energies for 80 elements in the periodic table, the electrochemical stability for the 23,776
11
12 ground state structures can already be determined.

13
14 We update the formalism of Persson *et al.*⁵ to include redox reactions corresponding to
15
16 an arbitrary metastable material. Metastable materials cannot result in thermodynamically
17
18 favorable redox reactions, thus, we estimate their Gibbs free energy difference with respect
19
20 to the Pourbaix stable domains as a function of pH and E , providing electrochemical insta-
21
22 bility maps for arbitrary metastable materials. This Gibbs free energy difference, ΔG_{pbx} ,
23
24 thus includes the instabilities arising from the enthalpy difference with respect to the likely
25
26 decomposition products of the metastable material at zero pressure and zero temperature,
27
28 also known as energy above the convex hull, ΔH_{solid} , and contributions from the pH and
29
30 voltage factors of Eq. 2. For a detailed information on the mathematical implementation,
31
32 please refer to the pymatgen python package.²³

33
34 As an example, Figure 1 shows the Pourbaix diagram of the Fe-V-O-H system with a 1:1
35
36 composition of Fe and V in an infinite reservoir of water. An ionic concentration of 10^{-5} M of
37
38 both Fe and V species, an activity of solids of 1, temperature of 298 K, and a pressure of 1 atm
39
40 is used for the analysis of Fe-V-O-H and all systems described henceforth, unless otherwise
41
42 noted. The ground state solids relevant to the Fe-V-O-H system, *i.e.* FeO, Fe₂O₃, Fe₃O₄,
43
44 Fe₂V₄O₁₃, Fe₃V, FeV, VO₂, V₂O₃, V₃O₄ and V₂O₅, are mapped in the Pourbaix diagram,
45
46 and their stability regions can be identified through inspection of the figure. However, the
47
48 metastable triclinic phase of FeVO₄ is not visibly represented in the equilibrium Pourbaix
49
50 diagram. Under ambient pressure, this phase exhibits a $\Delta H_{\text{solid}} = 0.34$ eV/atom for a 1:1
51
52 spontaneous decomposition to the stable Fe₂O₃ and Fe₂V₄O₁₃ solids. The ΔG_{pbx} with respect
53
54 to the Pourbaix stable domains, superimposed on the Pourbaix diagram, enables estimation
55
56 of the instability of FeVO₄ against all possible combinations of solid as well as aqueous
57
58
59
60

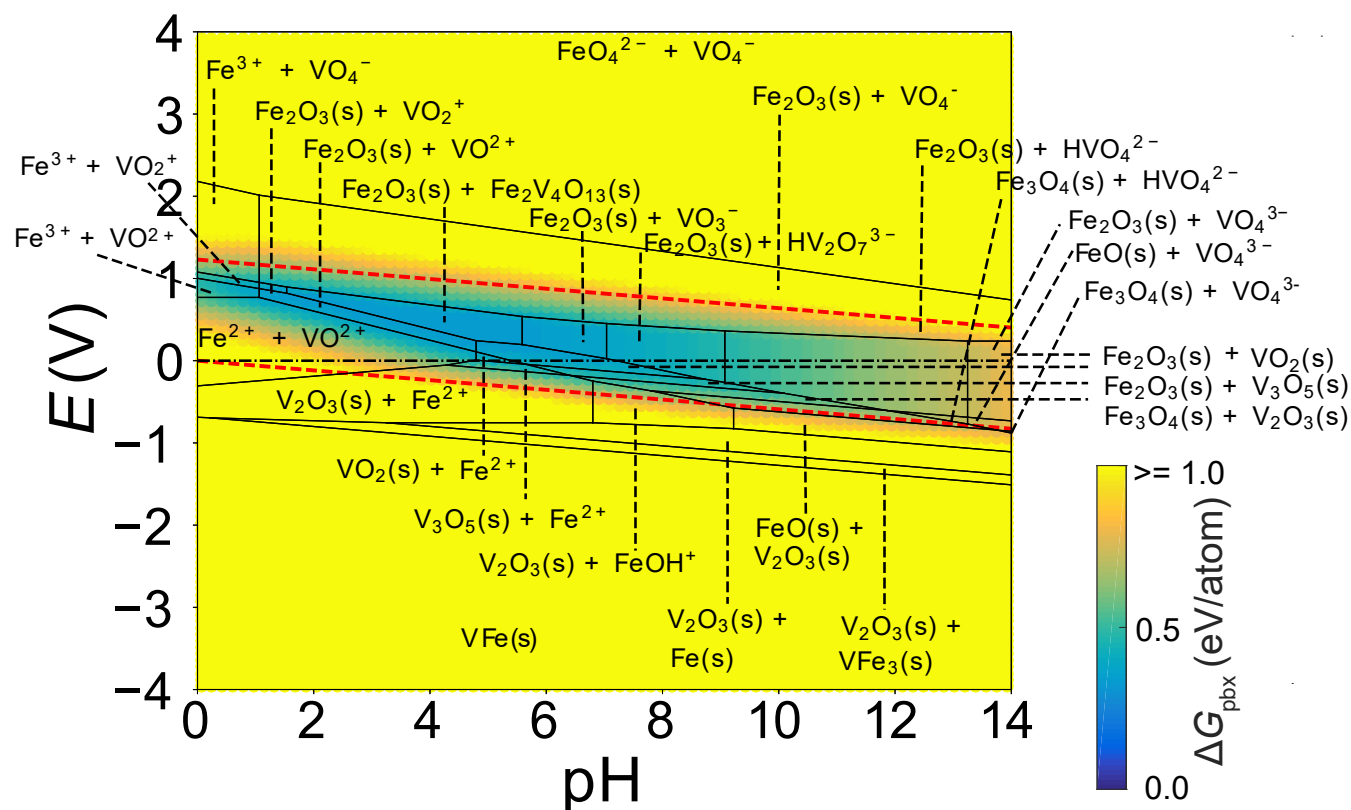


Figure 1: (Color online) Computationally predicted Pourbaix diagram of the Fe-V-O-H system. The Gibbs free energy, ΔG_{pbx} , of the metastable triclinic- FeVO_4 phase with respect to the Pourbaix stable phases is superimposed and represented by the colorbar. The lowest value of ΔG_{pbx} for FeVO_4 is 0.34 eV/atom at $\text{pH} = 1.63$ and voltage of $E = 0.85$ V, where it is predicted to phase transform to $\text{Fe}_2\text{V}_4\text{O}_{13}$ and Fe_2O_3 , a solid state reaction enabled by the stability of both reaction products under this electrochemical condition. The red dashed lines denote potentials of 0 V *vs* RHE and 1.23 V *vs* RHE.

1
2
3 species. We note that the most favorable ΔG_{pbx} for FeVO_4 occurs where it is expected to
4 decompose into $\text{Fe}_2\text{V}_4\text{O}_{13}$ and Fe_2O_3 in equal amounts to maintain the 1:1 stoichiometry of
5 Fe and V. The minimum of the $\Delta G_{\text{pbx}} = 0.34$ eV/atom is found at $\text{pH} = 1.63$ and $E = 1.85$
6 V, which includes the ΔH_{solid} and no contributions from the potential and pH factors are
7 expected based on the redox reactions. The ΔG_{pbx} increases rapidly beyond the stability
8 domain of $\text{Fe}_2\text{V}_4\text{O}_{13}$ and Fe_2O_3 indicating that it is progressively likely that the Pourbaix-
9 determined phases will be more favorable than the metastable FeVO_4 . Similar plots were
10 created for all the materials studied in this work.

11
12 In order to assess the ΔG_{pbx} which can be tolerated due to high barriers for solid-solid
13 phase transformations or mitigated by dissolution-precipitation-assisted surface passivation,
14 we compare the predicted ΔG_{pbx} with the electrochemical behavior of materials reported in
15 the experimental literature. In the next section we show examples of materials with ΔG_{pbx}
16 up to 0.5 eV/atom have been experimentally reported as stable within some observation
17 time. While the thermodynamic driving force for dissolution is an important metric, we
18 find that it is equally important to consider the nature of the decomposition products, e.g.
19 whether they form aqueous ions, solid phases or a combination thereof. For materials where
20 $\Delta G_{\text{pbx}} > 0$ and self-passivating layers form on the surface of the materials, we show that
21 the predicted passivation layer compositions are in agreement with experimentally observed
22 passivation layer compositions.

23
24 Methods for the model validation experiments are described in the Supporting Informa-
25 tion.
26
27

28 Results and Discussion

29 Validation Against Experimental Reports in the Literature

30
31 Figure 2 shows the theoretically computed ΔG_{pbx} for over 20 well known photoanode mate-
32 rials. We choose photoanode materials for a comparison of the theoretical predictions with
33
34
35
36
37
38
39
40
41
42
43
44
45
46
47
48
49
50
51
52
53
54
55
56
57
58
59
60

1
2
3
4 experimental reports in the literature since numerous studies report the electrochemical sta-
5
6 bility of photoanode materials. After the discovery of the first photoanode material in 1972,
7
8 TiO_2 ,²⁴ over 130 semiconductors, including oxides, sulphides and phosphides,¹¹ have been
9
10 extensively studied to improve, among other properties, their aqueous stability and opera-
11
12 tional life. The ΔG_{pbx} is computed for a potential of 1.5 V *vs* RHE (which accounts for the
13
14 1.23 eV free energy of water splitting and an overpotential of 0.27 eV that is typically re-
15
16 quired for electrocatalysis) and pH values corresponding to the experimental measurements
17
18 in the literature, Table 1.

19
20 The 12 metastable materials, anatase- TiO_2 , $\alpha\text{-Cu}_2\text{V}_2\text{O}_7$, $\alpha\text{-CuV}_2\text{O}_6$, BiVO_4 , $\gamma\text{-Cu}_3\text{V}_2\text{O}_8$,
21
22 BiFeO_3 , Fe_2TiO_5 , $\alpha\text{-Cu}_3\text{V}_2\text{O}_8$, $\text{Cu}_{11}\text{V}_6\text{O}_{26}$, CuWO_4 , FeV_2O_4 and FeVO_4 have ΔH_{solid} rang-
23
24 ing from 0.01 eV/atom, for anatase- TiO_2 , to 0.11 eV/atom, for FeVO_4 . The remaining
25
26 13 materials, $\text{Zn}(\text{FeO}_2)_2$, Bi_2MoO_6 , WO_3 , Fe_2O_3 , Bi_2WO_6 , $\text{Fe}_2\text{V}_4\text{O}_{13}$, $\beta\text{-Cu}_2\text{V}_2\text{O}_7$, WSe_2 ,
27
28 CdS , GaAs , InP , GaP and Si are thermodynamically stable materials, *i.e.* their $\Delta H_{\text{solid}} = 0$
29
30 eV/atom.

31
32 Evidently, the ΔG_{pbx} should be zero for the electrochemically stable compounds. How-
33
34 ever, somewhat surprisingly, excluding the spinel ZnFe_2O_4 and the orthorhombic WO_3 , all
35
36 the materials which are found to be stable experimentally have a $\Delta G_{\text{pbx}} > 0$, up to 0.5
37
38 eV/atom. Our calculations predict that WO_3 has a $\Delta G_{\text{pbx}} = 0$ for pH < 4 solutions and
39
40 it has also been reported to be stable experimentally at pH < 4.^{25,26} Further, at higher
41
42 pH values it has been observed to corrode, which is in agreement with the prediction that
43
44 the orthorhombic WO_3 should dissolve as WO_4^- ions with ΔG_{pbx} of up to 1 eV/atom. The
45
46 spinel structure of ZnFe_2O_4 has $\Delta G_{\text{pbx}} = 0$ eV/atom over a large alkaline range, pH = 7-14,
47
48 however, no experimental reports of the electrochemical stability could be identified in the
49
50 literature.^{27,28} For further details, see Figure S1 in the supporting information for pH de-
51
52 pendent ΔG_{pbx} and decomposition products of all the materials at 1.5 V (all voltages here
53
54 on are *vs* RHE).

55
56
57 Amongst those materials which exhibit a $\Delta G_{\text{pbx}} > 0$ but are still found to be stable
58
59
60

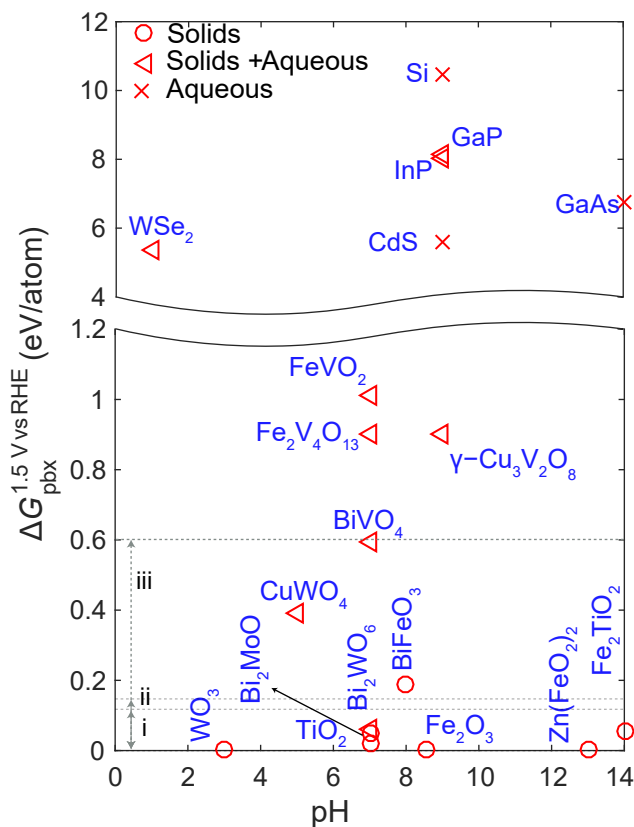


Figure 2: (Color online) The ΔG_{pbx} of photoanode materials at 1.5 V *vs* RHE at pH values corresponding to those in experimental reports, listed in Table 1. Materials which are expected to remain stable or decompose to only solid species are shown as circles. Those which decompose to solids as well as aqueous species are shown as triangles and the ones which are expected to dissociate to only aqueous species are shown as cross symbols. Refer Table 1 for details of the decomposed species. The driving forces to stabilize materials with energies marked in region (i) can be due to ionic concentration fluctuations, those marked in region (ii) could be due to temperature fluctuations and those by region (iii) due to activation energy barriers. Further, operational stability can also be obtained due to formation of inert passivation layers.

1
2
3 experimentally, Fe_2O_3 exhibits a $\Delta G_{\text{pbx}} = 0.001$ eV/atom at pH 2-12 which is within the
4 numerical accuracy of DFT. Experimental measurements are in excellent agreement showing
5 that Fe_2O_3 indeed exhibits a large pH stability window from 2-14.²⁹ The widely used pho-
6 toanode, anatase- TiO_2 , also has a small $\Delta G_{\text{pbx}} = 0.02$ eV/atom against the formation of its
7 polymorph α - TiO_2 . This small ΔG_{pbx} is found to be insufficient to drive a solid-solid phase
8 transformation and hence anatase- TiO_2 is found to be extremely robust in both alkaline
9 and acidic regions, pH = 0-14.^{30,31} Bi_2MoO_6 has a slightly larger $\Delta G_{\text{pbx}} = 0.05$ eV/atom and
10 is predicted to dissociate to Bi_4O_7 and MoO_4^- at pH = 7 and 1.4 V, but is found to be stable
11 experimentally.³² At pH = 7, Bi_2WO_6 has a $\Delta G_{\text{pbx}} = 0.06$ eV/atom, comparable to that
12 of Bi_2MoO_6 . Our formalism predicts a thermodynamic liability to dissociate to Bi_2O_4 and
13 WO_4^{2-} under these conditions. Yet, experimentally it has been observed to exhibit no sig-
14 nificant drop in photocurrent and no obvious change in the morphology.³³ Another material
15 which remains stable despite a $\Delta G_{\text{pbx}} > 0$ is FeBiO_3 , which at pH = 7.5 and 1.7 V is found
16 to be operationally stable despite the predicted dissociation into Fe_2O_3 and $\text{Bi}_4\text{O}_7^{-34,35}$ as
17 expected from our thermodynamic predictions. The most extreme of these examples is the
18 monoclinic scheelite BiVO_4 which has attracted recent interest due to conflicting reports of
19 aqueous stability. The material was deemed stable³⁶ at pH = 7 which corresponds to a very
20 large $\Delta G_{\text{pbx}} = 0.59$. Similarly, at pH = 6.6, $E = 1.41$ V, where $\Delta G_{\text{pbx}} = 0.45$ eV/atom,
21 no change in the X-ray diffraction (XRD) pattern or optical absorbance of BiVO_4 was ob-
22 served.³⁷ On the other hand, recent combined experimental and computational work shows
23 that BiVO_4 corrodes in alkaline pH at 1.23 V.³⁸

24
25
26
27
28
29
30
31
32
33
34
35
36
37
38
39
40
41
42
43
44
45
46 In contrast, materials with $\Delta G_{\text{pbx}} > 5.5$ eV/atom, *i.e.* Si, GaAs, InP, CdS and InP,
47 corrode vigorously.⁴⁹⁻⁵² We note that these five materials are predicted to either decompose
48 to only aqueous or a combination of oxides and aqueous species. None of them exhibit
49 instability to only solid phases. Consequently, these materials are coated with more stable
50 materials such as TiO_2 and Fe_2O_3 ^{31,53} when used as photoanodes.

51
52
53
54
55
56 All other examined materials are found to self-passivate with passivation layers whose
57
58
59
60

Table 1: The predicted stable species in aqueous media, Decomposed Species, and ΔG_{pbx} , in eV/atom, of 25 materials in water at 1.5 V *vs* RHE. The pH values, pH_{Exp} , correspond to the pH values in the measurements carried out in the listed references. The Materials Project material ids (mp-id) corresponding to the materials are listed as well.

Material	ΔG_{pbx}	pH_{Exp}	Decomposed Species	mp-id	Ref.
Zn(FeO ₂) ₂	0.00	13	Zn(FeO ₂) ₂ (s)	mp-19313	27,28
WO ₃	0.00	3	WO ₃ (s)	mp-19342	25
Fe ₂ O ₃	0.00	9	Fe ₂ O ₃ (s)	mp-24972	29,31
TiO ₂	0.02	7	TiO ₂ (s)	mp-390	30,31
Bi ₂ MoO ₆	0.05	7	Bi ₂ MoO ₆ (s)	mp-25708	32
Fe ₂ TiO ₅	0.06	14	Fe ₂ O ₃ (s) + TiO ₂ (s)	mp-24977	39
Bi ₂ WO ₆	0.06	7	Bi ₄ O ₇ (s) + WO ₄ ²⁻	mp-25730	33
BiFeO ₃	0.19	8	Fe ₂ O ₃ (s) + Bi ₄ O ₇ (s)	mp-24932	34,35
CuWO ₄	0.39	5	Cu ₂ O ₃ (s) + WO ₄ ²⁻	mp-510632	26,40
BiVO ₄	0.59	7	Bi ₄ O ₇ (s) + VO ₄ ⁻	mp-504878	36–38
Cu ₁₁ V ₆ O ₂₆	0.87	9	Cu ₂ O ₃ (s) + VO ₄ ⁻	mp-505456	7,41
Fe ₂ V ₄ O ₁₃	0.90	7	Fe ₂ O ₃ (s) + VO ₄ ⁻	mp-565529	42
γ -Cu ₃ V ₂ O ₈	0.90	9	Cu ₂ O ₃ (s) + VO ₄ ⁻	mp-504747	7,41,43
α -Cu ₃ V ₂ O ₈	0.92	9	Cu ₂ O ₃ (s) + VO ₄ ⁻	mp-600273	7,41
β -Cu ₂ V ₂ O ₇	1.00	9	Cu ₂ O ₃ (s) + VO ₄ ⁻	mp-559660	7,44
FeVO ₄	1.01	7	Fe ₂ O ₃ (s) + VO ₄ ⁻	mp-540630	45,46
α -Cu ₂ V ₂ O ₇	1.02	9	Cu ₂ O ₃ (s) + VO ₄ ⁻	mp-505508	7,44
α -CuV ₂ O ₆	1.28	9	Cu ₂ O ₃ (s) + VO ₄ ⁻	mp-741706	7,47
FeV ₂ O ₄	3.10	7	Fe ₂ O ₃ (s) + VO ₄ ⁻	mp-510496	45
WSe ₂	5.38	1	WO ₃ (s) + HSeO ₄ ⁻	mp-1821	48
CdS	5.58	9	Cd ²⁺ + SO ₄ ²⁻	mp-672	49,50
GaAs	6.77	14	AsO ₄ ³⁻ + GaO ₃ ³⁻	mp-2534	25,31,51,52
InP	8.01	9	In ₂ O ₃ (s) + HPO ₄ ²⁻	mp-20351	25,53
GaP	8.15	9	Ga ₂ O ₃ (s) + HPO ₄ ²⁻	mp-2490	25,31
Si	10.45	9	H ₄ SiO ₄ (aq)	mp-149	25,31

1
2
3 compositions are in excellent agreement with those predicted theoretically. For instance,
4
5 WSe₂ is predicted to dissociate to WO₃ and solvated Se atoms as HSeO₄⁻ ions with a ΔG_{pbx}
6
7 = 4.96 eV/atom at pH = 1 and $E = 1.43$ V, in excellent agreement with the experimental
8
9 observation that in perchloric acid, pH = 0.4-1.0, and at 1.43 V WSe₂ forms a thin porous
10
11 WO₃ passivation layer.⁴⁸ In another case, it is observed experimentally that mesoporous
12
13 films of Fe₂TiO₅ form self-passivating films composed of a mixture of mesoporous Fe₂TiO₅,
14
15 Fe₂O₃ and Fe-doped anatase-TiO₂³⁹ at pH = 13.9. Even though a direct comparison cannot
16
17 be made between the experiments for the mesoporous Fe₂TiO₅ and our calculations for
18
19 crystalline Fe₂TiO₅, we predict that crystalline Fe₂TiO₅ should indeed decompose to Fe₂O₃
20
21 and TiO₂ with a $\Delta G_{\text{pbx}} = 0.06$ eV/atom. Another class of materials, copper-vanadates, are
22
23 shown to form self-passivating layers in the alkaline region^{7,41,44} at pH = 7-13. This is in
24
25 agreement with the large ΔG_{pbx} of the Cu-vanadates, exceeding 1 eV/atom, and a prediction
26
27 that they dissociate to Cu₂O₃ and VO₄⁻ ions in aqueous solution.

28
29
30 Several other experimental reports provide an indirect evidence for the formation of self-
31
32 passivation layers. For example, FeV₂O₄ at pH = 7 is found to remain almost stable with
33
34 about 20 % change in current density at 1.0 V.⁴⁵ It is likely that the reduction in the current
35
36 density could be due to the formation of Fe₂O₃ passivation layers when V dissolves as VO₄⁻.
37
38 However, photodegradation and formation of solid electrolyte deposits could also be a cause
39
40 of the decrease in FeV₂O₄ film's current density. Similar Gibbs free energy based metric was
41
42 used to predict the aqueous stability of Li- and Na-based materials which are used as solid
43
44 electrolytes.⁵⁴ However, stability and passivation film composition were not verified due to
45
46 limited experimental literature.

47
48 Hence, we surmise that materials with ΔG_{pbx} up to high values of as much as 0.5
49
50 eV/atom can persist in electrochemical environments due to two possible reasons. Firstly,
51
52 the energy gained via dissociation to the Pourbaix stable domains may not be sufficient to
53
54 overcome the energy barrier for the dissociation reactions. Energy barriers for bulk solid state
55
56 transformations are found to be well below 1 eV/atom, greatly depending on the system under
57
58
59
60

1
2
3 consideration.^{55–58} Secondly, if the decomposition products include a major contribution from
4 solid state phase(s), preferential dissolution of some species can enable formation of a self-
5 passivating interphase, which will protect the underlying material. Furthermore, we note
6 that fluctuations in the ionic concentration and temperature can contribute significantly to
7 the corrosion/passivation process. For example, two orders of magnitude increase in the
8 ionic concentration can result in up to $2 \times 2.303 \times R T / F$ (0.118 eV/atom for $T = 298$
9 K or 0.128 eV/atom for $T = 323$ K) reduction in the decomposition energy. Considering
10 possible selective thermodynamic dissolution and precipitation of different species it is likely
11 that materials be immune to corrosion by self-passivation at ΔG_{pbx} energies which are of
12 the order of a fraction of an eV/atom. Needless to say the maximum ΔG_{pbx} up to which
13 a material is stable is very much dependent on the system and small changes in the ionic
14 concentration or small adjustments in pH and potential can be helpful in stabilizing materials.
15
16
17
18
19
20
21
22
23
24
25
26
27

28 While crystalline materials were used as inputs for the theoretical analysis, the experi-
29 mental reports of the 20 materials encompassed crystalline, amorphous and porous phases
30 synthesized under different conditions. These materials comprise different chemistries: ox-
31 ides, phosphides, sulphides, selenides and arsenides; and were investigated under different
32 electrolytes and electrolyte concentrations. In addition, while the photoanode surfaces were
33 characterized carefully in some reports, the stability and surface composition of several pho-
34 toanodes were more indirect.
35
36
37
38
39
40
41
42
43

44 Experimental Validation for Triclinic-FeVO₄

45
46
47 As further validation of our methodology and to explore the importance of our identification
48 and classification of decomposition products, we perform experiments based on the calcu-
49 lations of Fig. 1. A thin film of the metastable triclinic-FeVO₄, which has $\Delta H_{\text{solid}} = 0.11$
50 eV/atom, was grown via sputtering (see SI). We studied the elemental etch rates and surface
51 compositions before and after the electrochemical reactions at various voltages in an acidic
52 solution of pH = 2.9 and compared them to our calculations.
53
54
55
56
57
58
59
60

Table 2 shows the electrochemical response of FeVO_4 at this pH for various voltages as expected from our calculations. At voltages of -0.4 and 0.0 V FeVO_4 is expected to form a coating of bixbyite-type V_2O_3 concurrently losing Fe as Fe^{2+} ions. At the voltage of 0.4 V our calculations predict it to corrode into primarily Fe^{2+} and VO^{2+} ions. At a higher voltage of 0.8 V it is predicted to phase transform into monoclinic $\text{Fe}_2\text{V}_4\text{O}_{13}$ and $\alpha\text{-Fe}_2\text{O}_3$. Finally, at 1.2 V and 1.6 V a coating of $\alpha\text{-Fe}_2\text{O}_3$ is expected with loss of V as VO^{4-} ions.

Table 2: The predicted stable species in aqueous media, Decomposed Species, and ΔG_{pbx} of the triclinic- FeVO_4 in water at a pH of 2.9 and potentials, E , ranging from -0.4 V to 1.6 V vs RHE.

E vs RHE	ΔG_{pbx} eV/atom	Decomposed Species
-0.4	1.64	$\text{V}_2\text{O}_3(\text{s}) + \text{Fe}^{2+}$
0.0	1.04	$\text{V}_2\text{O}_3(\text{s}) + \text{Fe}^{2+}$
0.4	0.62	$\text{Fe}^{2+} + \text{VO}^{2+}$
0.8	0.34	$\text{Fe}_2\text{V}_4\text{O}_{13}(\text{s}) + \text{Fe}_2\text{O}_3(\text{s})$
1.2	0.59	$\text{Fe}_2\text{O}_3(\text{s}) + \text{VO}^{4-}$
1.6	0.99	$\text{Fe}_2\text{O}_3(\text{s}) + \text{VO}^{4-}$

A thin film composition library of $\text{Fe}_{1-x}\text{V}_x\text{O}_z$ was synthesized by combinatorial sputtering of Fe and V metal targets on fluorine doped tin oxide (FTO) coated glass substrate. The FeVO_4 phase pure regions in this composition library were determined using XRD. As expected, X-ray photoelectron spectroscopy (XPS, performed after air exposure) revealed the presence of Fe^{3+} and V^{+5} in these samples in approximately equal amounts (see Figure S3). In order to assess the electrochemical stability of these phase pure FeVO_4 samples, six as-deposited samples were polarized at -0.4, 0.0, 0.4, 0.8, 1.2, and 1.6 V respectively in an aqueous electrolyte solution buffered at pH 2.9 (0.1 M potassium phosphate, 0.04 M phosphoric acid with 0.25 M sodium sulfate) for 15 mins. In order to maintain a low ionic concentration in the solution over the course of this electrochemical process, it was performed in a scanning droplet cell with a rapid solution flow (approximately $0.5 \text{ L cm}^{-2} \text{ s}^{-1}$) over the working electrode. XRD-determined phases, the X-ray fluorescence(XRF)-determined molar concentrations of Fe and V and the XPS determined surface compositions were measured both before and after exposure to the aqueous electrochemical environment.

1
2
3
4
5
6
7
8
9
10
11
12
13
14
15
16
17
18
19
20
21
22
23
24
25
26
27
28
29
30
31
32
33
34
35
36
37
38
39
40
41
42
43
44
45
46
47
48
49
50
51
52
53
54
55
56
57
58
59
60

As the entire film thickness is within the sampling depth of XRF, comparison of the pre- and post-electrochemistry Fe and V molar concentrations provides an estimate of the average elemental etching rate during the experiments. Two example XRF spectra of films pre- and post-electrochemistry at potentials of 0.4 V and 0.8 V are shown in Figure 3(a) and (b), respectively. The V K- α and Fe K- α peaks were used for quantification of elemental concentrations and ultimately the average etch rates shown in Figure 4(a). At 0.4 V, about 50 % drop in the intensities of these peaks indicates that approximately half of the FeVO₄ film corroded away during the 15 minute experiment, which is also supported by the XRD characterization of the sample, see Figure S2, which shows the same FeVO₄ pattern but with approximately half the intensity in the post-electrochemistry measurement compared to the as-prepared measurement. The XPS signal from this sample (Figure S3) shows a peak corresponding to Sn from the FTO conducting layer, indicating that some regions of the thin film dissolved completely.

No change in FeVO₄ was observed in XRD characterization of the samples held at other potentials (Figure S2). However, the post-electrochemistry measurements included a signal from the electrolyte salt, indicating that upon drying the samples, some electrolyte salts precipitated on each sample's surface. As a result, Na, S and P were detected in the post-electrochemistry XRF signals, Figure 3. To understand the effect of the salt coating on the XRF measurement, we inspect the Si and Fe signals from the substrate and Sn signal from the FTO layer, whose slightly lowered intensity in the post-electrochemistry measurement demonstrates that the salt coating attenuates the XRF signal, resulting in a small apparent corrosion rate for both Fe and V even in the absence of corrosion. Consequently, Figure 4(a) provides an upper bound for the elemental etch rate of FeVO₄.

Only the 0.4 V sample exhibited substantial corrosion, which is consistent with the theoretical prediction that all decomposition products are solution-phase species at that condition. At all the remaining potentials, the elemental etch rates are nearly zero, in agreement with the theoretical results which predict that self-passivating coatings should be formed

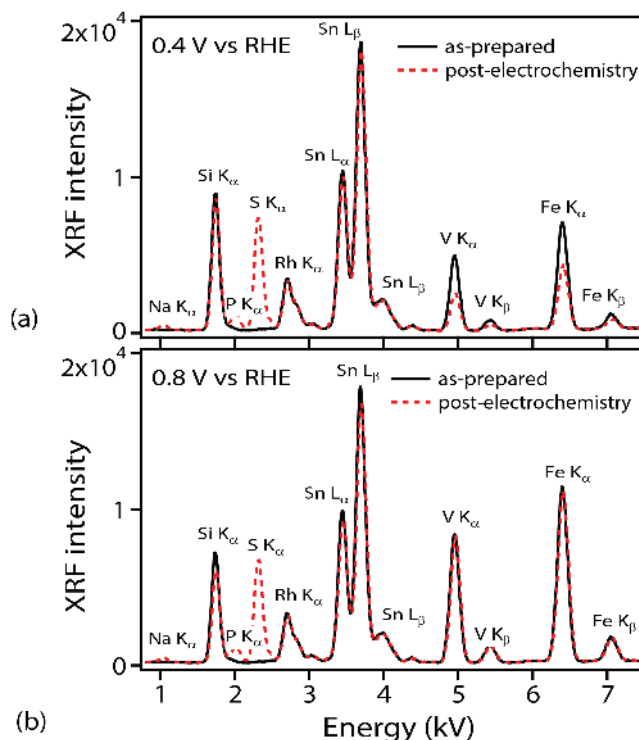


Figure 3: (Color online) XRF spectra for FeVO_4 sample before and after 15 mins electrochemical stability measurement in pH 2.9 under the potential of (a) 0.4 V and (b) 0.8 V *vs* RHE.

on the surface of FeVO_4 . At 0.8 V, the XRD signal shows (see Figure S2) that the FeVO_4 crystal structure was unchanged, indicating that the FeVO_4 most likely did not transform to the predicted solid products ($\text{Fe}_2\text{V}_4\text{O}_{13}$ and Fe_2O_3). This could possibly be due to the relatively low driving force ($\Delta G_{\text{pbx}} = 0.336$ eV/atom) for such a large solid-solid structural reorganization and no assistance from selective dissolution-precipitation processes as both Fe and V are predicted as stable against dissolution under these conditions.

The electrolyte salt coating on the electrochemically processed films resulted in relatively low Fe and V signals in the XPS spectra. The Fe 2*p* and V 2*p* XPS signals were compared with literature spectra for various species, indicating that the Fe^{3+} and V^{5+} species of the as-prepared film remain for films polarized at or above 0.8 V, which is commensurate with the prediction of phase stability and passivation by Fe_2O_3 in this voltage range. The films operated at -0.4 and 0 V contain lower-valent V, which is commensurate with the prediction of passivation by V_2O_3 under these conditions. Overall, these experiments demonstrate

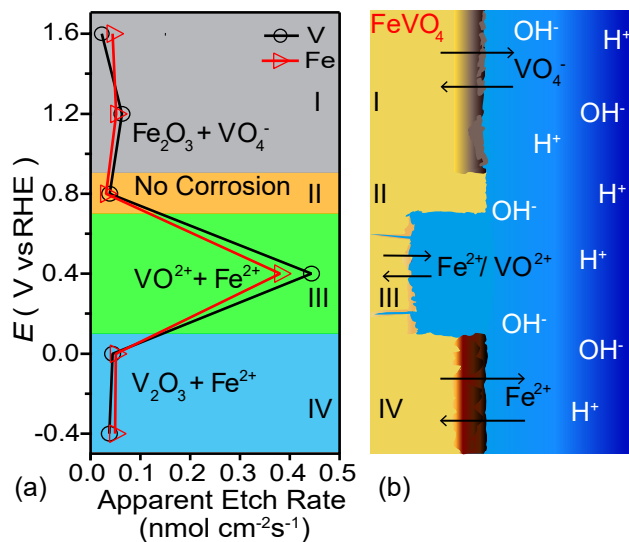


Figure 4: (Color online) (a) The etching rate of Fe and V over 15 min aqueous electrochemical operation at pH 2.9 as a function of applied potential. The calculated stable species in the 4 pertinent voltage ranges, I-IV, are shown in background color where corroding species are in bold italics. (b) A schematic of the morphology of FeVO₄ in presence of water under a steady state flow of the majority ions through the solid/liquid interface in regions I-IV corresponding to the voltage ranges marked in (a).

excellent agreement with the theoretical predictions and reveal that FeVO₄ does self-passivate at both low and high potential where a stable binary oxide is predicted to result from FeVO₄ decomposition.

Interestingly, at the potentials of -0.4 and 0 V, the XPS measurements show the presence of both Fe²⁺ and Fe³⁺ species (see Figure S3) in the film. The existence of Fe³⁺ species can be attributed to the pristine FeVO₄ bulk. However, the presence of Fe²⁺ species cannot be attributed to the formation of the V₂O₃ passivating layers or to the FeVO₄ bulk. In this context, we explain the presence of the Fe²⁺ species and the formation of the stable passivation layers using the concept of interfacial dissolution-precipitation processes and the Point Defect Model (PDM).^{16,59,60} The PDM postulates the existence of highly defective interfacial passivation layers (cation vacancies, cation interstitials, oxygen vacancies) that grow directly between the bulk and an exterior layer that forms via the hydrolysis of ions transmitted through the interfacial layer and the subsequent precipitation of a hydroxide,

oxyhydroxide or oxide depending upon the conditions. Under steady state conditions, the thickness of the passivation layer is controlled by the standard rate constants for the generation of the defects in the interfacial layer and dissolution of ions through the interfacial and outer layers. The presence of Fe^{2+} in the FeVO_4 samples operated at -0.4 and 0 V supports the interchange between the liquid and solid phase, as the stable aqueous species is Fe^{2+} . The highly defective interfacial and outer layers could contain both Fe^{2+} and Fe^{3+} species in interstitial sites or in a locally disordered Fe-V-O phase, see voltage range IV of Figure 4(b).

According to the PDM, while the formation of the passivating layers is a highly reactive thermodynamical process, the kinetic stability of the films is obtained through a steady state of defect generation and dissolution at the solid/passivation-layer/liquid interface. PDM predicts that the passivating films on FeVO_4 operated at 1.2 and 1.6 V are defective and disordered as well (see region I, Figure 4(b)), however, since the cations are in the same oxidation states both in the bulk material and the passivating films, XPS measurements are unable to corroborate the PDM predictions for this potential range. In total, all experimental results are commensurate with the model predictions.

Summary and Conclusions

In summary, we present a first-principles-based formalism to assess the propensity of thermodynamically stable as well as metastable materials towards electrochemical stabilization, passivation or corrosion in aqueous media. This formalism allows us to evaluate the relative Gibbs free energy, ΔG_{pbx} , of arbitrary materials with respect to Pourbaix stable species at any pH, voltage, temperature and concentration of ions. Comparing with experimental reports of 20 materials (including GaP, $\text{Zn}(\text{FeO}_2)_2$, Si, WSe_2 , GaAs, Fe_2O_3 , WO_3 and TiO_2) and our experimental investigations of the metastable triclinic- FeVO_4 , we show that materials predicted to have ΔG_{pbx} up to 0.5 eV/atom may remain stable in aqueous media, depending on the nature of their predicted decomposition products. High driving force for

1
2
3 decomposition (> 0.5 eV) and/or decomposition to only aqueous species is likely to cause
4 corrosion. On the other hand, materials that exhibit decomposition to both aqueous and
5 solid phases can exhibit self-passivation, by forming more stable solid phases at the interface.
6 In this context, we find an excellent agreement between experimentally measured and the-
7oretically predicted compositions of passivation layers for materials which form passivation
8 layers in water. Hence, the theoretical formalism presented here for estimating the electro-
9-chemical behavior of stable as well as metastable materials can be used to identify conditions
10 under which an arbitrary materials should form passivation layers and the composition of
11 these passivation layers. This *a priori* knowledge of the passivation film composition can
12 aid in parameterizing the Point Defect Model within the corrosion community. For instance,
13 once the passivation composition is known from our first-principles calculations, the defect
14 diffusion rates can be computed from atomistic simulations, such as DFT and molecular dy-
15 namics simulations. These parametrized PDM can be further used to predict the passivation
16 layer thickness and the electronic properties of the passivation layers.
17
18
19
20
21
22
23
24
25
26
27
28
29
30
31

32 Our work represents a clear advancement towards general corrosion management as well
33 as for optimizing operating conditions of aqueous-media-based applications like photoelectro-
34 catalysis. An open-source web-app based on the formalism is available at <https://materials>
35 [project.org](https://materials) which can be used to determine the electrochemical behavior of more than
36 69,000 materials available through the Materials Project database. Moreover, we make
37 the implementation of this formalism available via the Materials Project github repository
38 at <https://github.com/materials-project/pymatgen>, allowing the programmatic determina-
39 tion of electrochemical stability of arbitrary materials not included in the Materials Project
40 Database.
41
42
43
44
45
46
47
48
49
50
51

52 Acknowledgement

53
54
55 This work was primarily funded by the Joint Center for Artificial Photosynthesis, a DOE
56 Energy Innovation Hub, supported through the Office of Science of the U.S. Department of
57
58
59
60

1
2
3 Energy under Award Number DE-SC0004993. Computational work was additionally sup-
4 ported by the Materials Project (Grant No. EDCBEE) Predictive Modeling Center through
5 the US Department of Energy (DOE), Office of Basic Energy Sciences, Materials Sciences
6 and Engineering Division, under Contract DE-AC02-05CH11231. Computational resources
7 were provided by the National Energy Research Scientific Computing Center, a DOE Office
8 of Science User Facility supported by the Office of Science of the U.S. Department of En-
9 ergy under Contract No. DE-AC02-05CH11231. The authors thank Matthias Richter for
10 assistance with collection of XPS data.
11
12
13
14
15
16
17
18
19

20 21 Supporting Information Available

22 See supporting information for the pH dependent ΔG_{pbx} and decomposition products of all
23 the photoanode materials at 1.5 V, physical vapor deposition based synthesis procedure of
24 FeVO₄, pre- and post-electrochemistry phase-identification by XRD, composition measure-
25 ments by XRF and near-surface chemistry measurement by XPS. This material is available
26 free of charge via the Internet at <http://pubs.acs.org/>.
27
28
29
30
31
32
33
34
35

36 37 References

- 38
39 (1) Koch, G. H.; Brongers, M. P.; Thompson, N. G.; Virmani, Y. P.; Payer, J. H. *Corrosion*
40 *cost and preventive strategies in the United States*; 2002.
41
42
43
44 (2) Pourbaix, M. Atlas of electrochemical equilibria in aqueous solutions. **1974**,
45
46
47 (3) Takeno, N. Atlas of Eh-pH diagrams. *Geological survey of Japan open file report* **2005**,
48 *419*, 102.
49
50
51
52 (4) Brookins, D. G. *Eh-pH diagrams for geochemistry*; Springer Science & Business Media,
53 2012.
54
55
56
57 (5) Persson, K. A.; Waldwick, B.; Lazic, P.; Ceder, G. Prediction of solid-aqueous equilibria:
58
59
60

- Scheme to combine first-principles calculations of solids with experimental aqueous states. *Phys. Rev. B* **2012**, *85*, 235438.
- (6) Yan, Q.; Li, G.; Newhouse, P. F.; Yu, J.; Persson, K. A.; Gregoire, J. M.; Neaton, J. B. $\text{Mn}_2\text{V}_2\text{O}_7$: An earth abundant light absorber for solar water splitting. *Adv. Energy Mater.* **2015**, *5*.
- (7) Zhou, L.; Yan, Q.; Yu, J.; Jones, R. J.; Becerra-Stasiewicz, N.; Suram, S. K.; Shinde, A.; Guevarra, D.; Neaton, J. B.; Persson, K. A.; Gregoire, J. M. Stability and self-passivation of copper vanadate photoanodes under chemical, electrochemical, and photoelectrochemical operation. *Phys. Chem. Chem. Phys.* **2016**, *18*, 9349–9352.
- (8) Wills, L. A.; Qu, X.; Chang, I.-Y.; Mustard, T. J.; Keszler, D. A.; Persson, K. A.; Cheong, P. H.-Y. Group additivity-Pourbaix diagrams advocate thermodynamically stable nanoscale clusters in aqueous environments. *Nat. Commun.* **2017**, *8*.
- (9) Koyama, M.; Zhang, Z.; Wang, M.; Ponge, D.; Raabe, D.; Tsuzaki, K.; Noguchi, H.; Tasan, C. C. Bone-like crack resistance in hierarchical metastable nanolaminate steels. *Science* **2017**, *355*, 1055–1057.
- (10) Kazemi, F.; Saberi, A.; Malek-Ahmadi, S.; Sohrabi, S.; Rezaie, H.; Tahriri, M. Novel method for synthesis of metastable tetragonal zirconia nanopowders at low temperatures. *Ceram.-Silik.* **2011**, *55*, 26–30.
- (11) Singh, A. K.; Mathew, K.; Zhuang, H. L.; Hennig, R. G. Computational screening of 2D materials for photocatalysis. *J. Phys. Chem. Lett.* **2015**, *6*, 1087–1098.
- (12) Luo, G.; Yang, S.; Jenness, G. R.; Song, Z.; Kuech, T. F.; Morgan, D. Understanding and reducing deleterious defects in metastable alloy GaAsBi. *NPG Asia Mater.* **2016**, *9*, e345.

- 1
2
3
4 (13) Belsky, A.; Hellenbrandt, M.; Karen, V. L.; Luksch, P. New developments in the Inor-
5 ganic Crystal Structure Database (ICSD): accessibility in support of materials research
6 and design. *Acta Crystallogr., Sect. B: Struct. Sci.* **2002**, *58*, 364–369.
7
8
9
10 (14) Sun, W.; Dacek, S. T.; Ong, S. P.; Hautier, G.; Jain, A.; Richards, W. D.; Gamst, A. C.;
11 Persson, K. A.; Ceder, G. The thermodynamic scale of inorganic crystalline metasta-
12 bility. *Sci. Adv.* **2016**, *2*, e1600225.
13
14
15
16
17 (15) Wagman, D. D.; Evans, W. H.; Parker, V. B.; Schumm, R. H.; Halow, I. *The NBS*
18 *tables of chemical thermodynamic properties. Selected values for inorganic and C1 and*
19 *C2 organic substances in SI units*; 1982.
20
21
22
23
24 (16) Macdonald, D. On the existence of our metals based civilization. I. Phase-space analysis.
25 2006. *J. Electrochem. Soc.* **2006**, *157(7)* B213-B224.
26
27
28
29 (17) Jain, A.; Ong, S. P.; Hautier, G.; Chen, W.; Richards, W. D.; Dacek, S.; Cholia, S.;
30 Gunter, D.; Skinner, D.; Ceder, G.; Persson, K. a. The Materials Project: A materials
31 genome approach to accelerating materials innovation. *APL Mater.* **2013**, *1*, 011002.
32
33
34
35
36 (18) Saal, J. E.; Kirklin, S.; Aykol, M.; Meredig, B.; Wolverton, C. Materials design and
37 discovery with high-throughput density functional theory: the open quantum materials
38 database (OQMD). *JOM* **2013**, *65*, 1501–1509.
39
40
41
42
43 (19) Curtarolo, S.; Setyawan, W.; Wang, S.; Xue, J.; Yang, K.; Taylor, R. H.; Nel-
44 son, L. J.; Hart, G. L.; Sanvito, S.; Buongiorno-Nardelli, M.; Mingo, N.; Levy, O.
45 AFLOWLIB.ORG: A distributed materials properties repository from high-throughput
46 ab initio calculations. *Comput. Mater. Sci.* **2012**, *58*, 227–235.
47
48
49
50
51
52 (20) Bale, C.; Béliisle, E.; Chartrand, P.; Deckerov, S.; Eriksson, G.; Gheribi, A.; Hack, K.;
53 Jung, I.-H.; Kang, Y.-B.; Melançon, J.; Peltron, A.; Petersen, S.; Robelin, C.; Sang-
54 ster, J.; Spencer, P.; VanEnde, M-A. FactSage thermochemical software and databases,
55 2010–2016. *Calphad* **2016**, *54*, 35–53.
56
57
58
59
60

- 1
2
3
4
5
6
7
8
9
10
11
12
13
14
15
16
17
18
19
20
21
22
23
24
25
26
27
28
29
30
31
32
33
34
35
36
37
38
39
40
41
42
43
44
45
46
47
48
49
50
51
52
53
54
55
56
57
58
59
60
- (21) Johnson, J. W.; Oelkers, E. H.; Helgeson, H. C. SUPCRT92: A software package for calculating the standard molal thermodynamic properties of minerals, gases, aqueous species, and reactions from 1 to 5000 bar and 0 to 1000 C. *Comput. Geosci.* **1992**, *18*, 899–947.
- (22) Ong, S. P.; Cholia, S.; Jain, A.; Brafman, M.; Gunter, D.; Ceder, G.; Persson, K. A. The Materials Application Programming Interface (API): A simple, flexible and efficient API for materials data based on REpresentational State Transfer (REST) principles. *Comput. Mater. Sci.* **2015**, *97*, 209–215.
- (23) Ong, S. P.; Richards, W. D.; Jain, A.; Hautier, G.; Kocher, M.; Cholia, S.; Gunter, D.; Chevrier, V. L.; Persson, K. A.; Ceder, G. Python Materials Genomics (pymatgen): A robust, open-source python library for materials analysis. *Comput. Mater. Sci.* **2013**, *68*, 314–319.
- (24) Fujishima, A.; Honda, K. Electrochemical photolysis of water at a semiconductor electrode. *Nature* **1972**, *238*, 37–38.
- (25) Liu, R.; Zheng, Z.; Spurgeon, J.; Yang, X. Enhanced photoelectrochemical water-splitting performance of semiconductors by surface passivation layers. *Energy Environ. Sci.* **2014**, *7*, 2504–2517.
- (26) Yourey, J. E.; Pyper, K. J.; Kurtz, J. B.; Bartlett, B. M. Chemical stability of CuWO₄ for photoelectrochemical water oxidation. *J. Phys. Chem. C* **2013**, *117*, 8708–8718.
- (27) Valenzuela, M.; Bosch, P.; Jiménez-Becerrill, J.; Quiroz, O.; Páez, A. Preparation, characterization and photocatalytic activity of ZnO, Fe₂O₃ and ZnFe₂O₄. *J. Photochem. Photobiol. , A* **2002**, *148*, 177–182.
- (28) De Haart, L.; Blasse, G. Photoelectrochemical properties of ferrites with the spinel structure. *J. Electrochem. Soc.* **1985**, *132*, 2933–2938.

- 1
2
3 (29) Beverskog, B.; Puigdomenech, I. Revised Pourbaix diagrams for iron at 25–300 °C.
4
5 *Corros. Sci.* **1996**, *38*, 2121–2135.
6
7
8 (30) Ni, M.; Leung, M. K.; Leung, D. Y.; Sumathy, K. A review and recent developments
9
10 in photocatalytic water-splitting using TiO₂ for hydrogen production. *Renewable Sus-*
11
12 *tainable Energy Rev.* **2007**, *11*, 401–425.
13
14
15 (31) Hu, S.; Shaner, M. R.; Beardslee, J. A.; Lichterman, M.; Brunschwig, B. S.; Lewis, N. S.
16
17 Amorphous TiO₂ coatings stabilize Si, GaAs, and GaP photoanodes for efficient water
18
19 oxidation. *Science* **2014**, *344*, 1005–1009.
20
21
22 (32) Tang, D.; Mabayoje, O.; Lai, Y.; Liu, Y.; Mullins, C. B. Enhanced Photoelectrochemi-
23
24 cal Performance of Porous Bi₂MoO₆ Photoanode by an Electrochemical Treatment. *J.*
25
26 *Electrochem. Soc.* **2017**, *164*, H299–H306.
27
28
29 (33) Zhang, L.; Baumanis, C.; Robben, L.; Kandiel, T.; Bahnemann, D. Bi₂WO₆ Inverse
30
31 Opals: Facile Fabrication and Efficient Visible-Light-Driven Photocatalytic and Pho-
32
33 toelectrochemical Water-Splitting Activity. *Small* **2011**, *7*, 2714–2720.
34
35
36 (34) Chen, X.; Yu, T.; Gao, F.; Zhang, H.; Liu, L.; Wang, Y.; Li, Z.; Zou, Z.; Liu, J.-M.
37
38 Application of weak ferromagnetic BiFeO₃ films as the photoelectrode material under
39
40 visible-light irradiation. *Appl. Phys. Lett.* **2007**, *91*, 022114.
41
42
43 (35) Moniz, S. J.; Quesada-Cabrera, R.; Blackman, C. S.; Tang, J.; Southern, P.;
44
45 Weaver, P. M.; Carmalt, C. J. A simple, low-cost CVD route to thin films of BiFeO₃
46
47 for efficient water photo-oxidation. *J. Mater. Chem. A* **2014**, *2*, 2922–2927.
48
49
50 (36) Tolod, K. R.; Hernández, S.; Russo, N. Recent advances in the BiVO₄ photocatalyst
51
52 for sun-driven water oxidation: Top-performing photoanodes and scale-up challenges.
53
54 *Catalysts* **2017**, *7*, 13.
55
56
57
58
59
60

- 1
2
3
4
5
6
7
8
9
10
11
12
13
14
15
16
17
18
19
20
21
22
23
24
25
26
27
28
29
30
31
32
33
34
35
36
37
38
39
40
41
42
43
44
45
46
47
48
49
50
51
52
53
54
55
56
57
58
59
60
- (37) Sayama, K.; Nomura, A.; Zou, Z.; Abe, R.; Abe, Y.; Arakawa, H. Photoelectrochemical decomposition of water on nanocrystalline BiVO₄ film electrodes under visible light. *Chem. Commun.* **2003**, 2908–2909.
- (38) Toma, F. M. et al. Mechanistic insights into chemical and photochemical transformations of bismuth vanadate photoanodes. *Nat. Commun.* **2016**, 7.
- (39) Courtin, E.; Baldinozzi, G.; Sougrati, M. T.; Stievano, L.; Sanchez, C.; Laberty-Robert, C. New Fe₂TiO₅-based nanoheterostructured mesoporous photoanodes with improved visible light photoresponses. *J. Mater. Chem. A* **2014**, 2, 6567–6577.
- (40) Doumerc, J.-P.; Hejtmanek, J.; Chaminade, J.-P.; Pouchard, M.; Krussanova, M. A photoelectrochemical study of CuWO₄ single crystals. *Phys. Status Solidi A* **1984**, 82, 285–294.
- (41) Nandjou, F.; Haussener, S. Degradation in photoelectrochemical devices: review with an illustrative case study. *J. Phys. D: Appl. Phys.* **2017**, 50, 124002.
- (42) Tang, D.; Rettie, A. J.; Mabayoje, O.; Wygant, B. R.; Lai, Y.; Liu, Y.; Mullins, C. B. Facile growth of porous Fe₂V₄O₁₃ films for photoelectrochemical water oxidation. *J. Mater. Chem. A* **2016**, 4, 3034–3042.
- (43) Seabold, J. A.; Neale, N. R. All first row transition metal oxide photoanode for water splitting based on Cu₃V₂O₈. *Chem. Mater.* **2015**, 27, 1005–1013.
- (44) Kalal, S.; Pandey, A.; Ameta, R.; Punjabi, P. B. Heterogeneous photo-Fenton-like catalysts Cu₂V₂O₇ and Cr₂V₄O₁₃ for an efficient removal of azo dye in water. *Cogent Chem.* **2016**, 2, 1143344.
- (45) Mandal, H.; Shyamal, S.; Hajra, P.; Bera, A.; Sariket, D.; Kundu, S.; Bhattacharya, C. Development of ternary iron vanadium oxide semiconductors for applications in photoelectrochemical water oxidation. *RSC Adv.* **2016**, 6, 4992–4999.

- 1
2
3
4 (46) Morton, C. D.; Slipper, I. J.; Thomas, M. J.; Alexander, B. D. Synthesis and charac-
5 terisation of Fe-V-O thin film photoanodes. *J. Photochem. Photobiol., A* **2010**, *216*,
6 209–214.
7
8
9
10 (47) Guo, W.; Chemelewski, W. D.; Mabayoje, O.; Xiao, P.; Zhang, Y.; Mullins, C. B.
11 Synthesis and characterization of CuV_2O_6 and $\text{Cu}_2\text{V}_2\text{O}_7$: Two photoanode candidates
12 for photoelectrochemical water oxidation. *J. Phys. Chem. C* **2015**, *119*, 27220–27227.
13
14
15
16
17 (48) Tenne, R.; Wold, A. Passivation of recombination centers in $n\text{-WSe}_2$ yields high effi-
18 ciency ($> 14\%$) photoelectrochemical cell. *Appl. Phys. Lett.* **1985**, *47*, 707–709.
19
20
21
22 (49) Meissner, D.; Benndorf, C.; Memming, R. Photocorrosion of cadmium sulfide: Analysis
23 by photoelectron spectroscopy. *Appl. Surf. Sci.* **1987**, *27*, 423–436.
24
25
26
27 (50) Yamada, S.; Nosaka, A. Y.; Nosaka, Y. Fabrication of CdS photoelectrodes coated with
28 titania nanosheets for water splitting with visible light. *J. Electroanal. Chem.* **2005**,
29 *585*, 105–112.
30
31
32
33
34 (51) Schmuki, P.; Sproule, G.; Bardwell, J.; Lu, Z.; Graham, M. Thin anodic oxides formed
35 on GaAs in aqueous solutions. *J. Appl. Phys.* **1996**, *79*, 7303–7311.
36
37
38
39 (52) Wang, H.-H.; Wu, J.-Y.; Wang, Y.-H.; Houng, M.-P. Effects of pH Values on the
40 Kinetics of Liquid-Phase Chemical-Enhanced Oxidation of GaAs. *J. Electrochem. Soc.*
41 **1999**, *146*, 2328–2332.
42
43
44
45
46 (53) Lee, M. H.; Takei, K.; Zhang, J.; Kapadia, R.; Zheng, M.; Chen, Y.-Z.; Nah, J.;
47 Matthews, T. S.; Chueh, Y.-L.; Ager, J. W.; Javey, A. p -Type InP Nanopillar Pho-
48 to cathodes for Efficient Solar-Driven Hydrogen Production. *Angew. Chem., Int. Ed.*
49 **2012**, *51*, 10760–10764.
50
51
52
53
54
55 (54) Radhakrishnan, B.; Ong, S. P. Aqueous stability of alkali superionic conductors from
56 first-principles calculations. *Frontiers in Energy Research* **2016**, *4*, 16.
57
58
59
60

- 1
2
3
4 (55) Lian, X.; Xiao, P.; Liu, R.; Henkelman, G. Calculations of oxygen adsorption-induced
5 surface reconstruction and oxide formation on Cu (100). *Chem. Mater.* **2017**, *29*, 1472–
6 1484.
7
8
9
10 (56) Duan, Z.; Henkelman, G. CO oxidation on the Pd (111) surface. *ACS Catal.* **2014**, *4*,
11 3435–3443.
12
13
14
15 (57) Barmak, K.; Liu, J.; Harlan, L.; Xiao, P.; Duncan, J.; Henkelman, G. Transforma-
16 tion of topologically close-packed β -W to body-centered cubic α -W: Comparison of
17 experiments and computations. *J. Chem. Phys.* **2017**, *147*, 152709.
18
19
20
21
22 (58) Guo, Y.; Sun, D.; Ouyang, B.; Raja, A.; Song, J.; Heinz, T. F.; Brus, L. E. Probing the
23 dynamics of the metallic-to-semiconducting structural phase transformation in MoS₂
24 crystals. *Nano Lett.* **2015**, *15*, 5081–5088.
25
26
27
28
29 (59) Macdonald, D. D. Theory of passive film stability. *ECS Trans.* **2007**, *2*, 73–81.
30
31
32 (60) Obot, I.; Macdonald, D.; Gasem, Z. Density functional theory (DFT) as a powerful
33 tool for designing new organic corrosion inhibitors. Part 1: an overview. *Corros. Sci.*
34 **2015**, *99*, 1–30.
35
36
37
38
39
40
41
42
43
44
45
46
47
48
49
50
51
52
53
54
55
56
57
58
59
60

Graphical TOC Entry

